

Dust Destruction in Type Ia Supernova Remnants in the Large Magellanic Cloud

Kazimierz J. Borkowski,¹ Brian J. Williams,¹ Stephen P. Reynolds,¹ William P. Blair,² Parviz Ghavamian,² Ravi Sankrit,² Sean P. Hendrick,³ Knox S. Long,⁴ John C. Raymond,⁵ R. Chris Smith,⁶ Sean Points,⁶ & P. Frank Winkler⁷

ABSTRACT

We present first results from an extensive survey of Magellanic Clouds supernova remnants (SNRs) with the *Spitzer Space Telescope*. We describe IRAC and MIPS imaging observations at 3.6, 4.5, 5.8, 8, 24, and 70 μm of four Balmer-dominated Type Ia SNRs in the Large Magellanic Cloud (LMC): DEM L71 (0505-67.9), 0509-67.5, 0519-69.0, and 0548-70.4. None was detected in the four short-wavelength IRAC bands, but all four were clearly imaged at 24 μm , and two at 70 μm . A comparison of these images to *Chandra* broadband X-ray images shows a clear association with the blast wave, and not with internal X-ray emission associated with ejecta. Our observations are well described by 1-D shock models of collisionally heated dust emission, including grain size distributions appropriate for the LMC, grain heating by collisions with both ions and electrons, and sputtering of small grains. Model parameters are constrained by X-ray, optical, and far-ultraviolet observations. Our models can reproduce observed 70/24 μm flux ratios only by including sputtering, destroying most grains smaller than 0.03–0.04 μm in radius. We infer total dust masses swept up by the SNR blast waves, before sputtering, of order $10^{-2} M_{\odot}$, several times less than

¹Physics Dept., North Carolina State U., Raleigh, NC 27695-8202; kborkow@ncsu.edu, steve_reynolds@ncsu.edu, bjwilli2@ncsu.edu

²Dept. of Physics and Astronomy, Johns Hopkins, 3400 N. Charles St., Baltimore, MD 21218-2686; wpb@pha.jhu.edu, parviz@pha.jhu.edu, ravi@pha.jhu.edu

³Physics Dept., Millersville U., PO Box 1002, Millersville, PA 17551; sean.hendrick@millersville.edu

⁴STScI, 3700 San Martin Dr., Baltimore, MD 21218; long@stsci.edu

⁵Harvard-Smithsonian Center for Astrophysics, 60 Garden Street, Cambridge, MA 02138; jraymond@cfa.harvard.edu

⁶CTIO, Cailla 603, La Serena, Chile; csmith@noao.edu, spoints@noao.edu

⁷Dept. of Physics, Middlebury College, Middlebury, VT 05753; winkler@middlebury.edu

those implied by a dust/gas mass ratio of 0.3% as often assumed for the LMC. Substantial dust destruction has implications for gas-phase abundances.

Subject headings: interstellar medium: dust — supernova remnants — Magellanic Clouds

1. Introduction

The dust content in galaxies, dust composition, and grain size distribution are determined by the balance between dust formation, modification in the interstellar medium (ISM), and destruction (Draine 2003). Some evidence exists for dust formation in the ejecta of core-collapse supernovae (e.g., SN 1987A; de Kool, Li, & McCray 1998) but no reports exist for SNe Ia. Dust *destruction* is intrinsically linked to SN activity, through sputtering in gas heated by energetic blast waves and through betatron acceleration in radiative shocks (Jones 2004). Dust destruction in SNRs can be studied by its strong influence on thermal IR emission from collisionally heated dust. The IRAS All Sky Survey provided fundamental data on Galactic SNRs (Arendt 1989; Saken, Shull, & Fesen 1992). This prompted extensive theoretical work on dust heating, emission, and destruction within hot plasmas, summarized by Dwek & Arendt (1992). Theory is broadly consistent with IRAS observations, but limitations of those observations (low spatial and spectral resolution and confusion with the Galactic IR background) precluded any detailed comparisons. In particular, while it is clear that thermal dust emission is prevalent in SNRs, our understanding of dust destruction is quite poor.

To examine the nature of dust heating and destruction in the interstellar medium, we conducted an imaging survey with the *Spitzer Space Telescope* (SST) of 39 SNRs in the Magellanic Clouds (MCs). We have selected a subset of our detections, four remnants of Type Ia supernovae, to address questions of dust formation in Type Ia ejecta, dust content of the diffuse ISM of the LMC, and dust destruction in SNR shocks. Both DEM L71 (0505-67.9; Rakowski, Ghavamian, & Hughes 2003) and 0548-70.4 (Hendrick, Borkowski, & Reynolds 2003) show X-ray evidence for iron-rich ejecta in the interior, and both have well-studied Balmer emission from nonradiative shocks (Ghavamian et al. 2003; Smith et al. 1991). Two smaller remnants, 0509-67.5 and 0519-69.0, also show prominent H α and Ly β emission from nonradiative shocks (Tuohy et al. 1982; Smith et al. 1991; Ghavamian et al. 2006, in preparation). There appears to be little or no optical contribution from radiative shocks. Confusion in IR is widespread in the LMC, but our remnants are less confused than typical, easing the task of separating SNR emission from background.

2. Observations and Data Reduction

We observed all four objects in all four bands of the Infrared Array Camera (IRAC), as well as with the Multiband Imaging Photometer for Spitzer (MIPS) at 24, 70, and 160 μm . The 160 μm images contain only emission from the general ISM, so we do not discuss them here. Each IRAC observation totaled 300 s (10 30-s frames); at 24 μm , 433 s total (14 frames); and at 70 μm , 986 s total (94 frames) for all but 0548–70.4, for which we observed a total of 546 s in 52 frames. The observations took place between November 2004 and April 2005. Images are shown in Figure 1. Confusion from widely distributed warm dust made many 70 μm observations problematic, but we obtained useful data on both DEM L71 and 0548–70.4.

MIPS images were processed from Basic Calibrated Data (BCD) to Post-BCD (PBCD) by v. 11 of the SSC PBCD pipeline. For the 24 μm images, we then re-mosaicked the stack of BCD images into a PBCD mosaic using the SSC-provided software MOPEX, specifically the overlap correction, to rid the images of artifacts. For the 70 μm data, we used the contributed software package GeRT, provided also by the SSC, to remove some vertical streaking. IRAC images were also reprocessed using MOPEX to rid the image of artifacts caused by bright stars.

All four remnants were clearly detected at 24 μm , with fluxes from indicated regions reported in Table 1. As Figure 1 shows, emission is clearly associated with the X-ray-delineated blast wave, though not with interior X-ray emission. Since we expect line emission from fine-structure transitions of low-ionization material to be a significant contributor only in cooler, denser regions identified by radiative shocks, we conclude that the emission we detect is predominantly from heated dust. None of our objects was clearly detected at 8 μm , with fairly stringent upper limits shown in Table 1.

3. Discussion

We modeled the observed emission assuming collisionally heated dust (e.g., Dwek & Arendt 1992). The models allow an arbitrary grain-size distribution, and require as input parameters the hot gas density n , electron temperature T_e , ion temperature T_i , and shock sputtering age $\tau = \int_0^t n_p dt$. The models use an improved version of the code described by Borkowski et al. (1994), including a method devised by Guhathakurta & Draine (1989) to account for transiently-heated grains, whose temperature fluctuates with time and therefore radiate far more efficiently. The energy deposition rates by electrons and protons were calculated according to Dwek (1987) and Dwek & Smith (1996). We used dust emissivi-

ties based on bulk optical constants of Draine & Lee (1984). Our non-detections in IRAC bands showed that small grains are destroyed, so it was not necessary to model emission features from small polycyclic aromatic hydrocarbon (PAH) grains. The preshock grain size distribution was taken from the “provisional” dust model of Weingartner & Draine (2001), consisting of separate carbonaceous and silicate grain populations, in particular their average LMC model with maximal amount of small carbonaceous grains. Sputtering rates are based on sputtering cross sections of Bianchi & Ferrara (2005), augmented by calculations of an enhancement in sputtering yields for small grains by Jurac, Johnson, & Donn (1998). We have modeled 1-D shocks, that is, superposed emission from regions of varying sputtering age from zero up to a specified shock age (Dwek, Foster, & Vancura 1996).

To estimate shock parameters, we used the non-radiative shock models of Ghavamian et al. (2001) to model the broad component $H\alpha$ widths and broad-to-narrow $H\alpha$ flux ratios measured by Tuohy et al. (1982) and Smith et al. (1991) for the LMC SNRs. Results for electron and proton temperatures T_e and T_p are quoted in Table 2. For 0509–67.5, we assumed $T_e/T_p \leq 0.1$ at the shock front, consistent with the observed $Ly\beta$ FWHM of 3700 km s^{-1} (Ghavamian et al. 2006, in preparation). For Sedov dynamics, the sputtering age τ (which is also the ionization timescale) reaches a maximum of about $(1/3)n_p t$ where t is the true age of the blast wave (Borkowski, Lyerly, & Reynolds 2001). Therefore we use an “effective sputtering age” of $n_p t/3$ when calculating effects of sputtering.

3.1. DEM L71 and 0548–70.4

These two remnants have been well-studied in X-rays (DEM L71: Rakowski et al. 2003; 0548–70.4, Hendrick et al. 2003). They have ages of 4400 and 7100 yr, respectively, derived from Sedov models. For DEM L71, Ghavamian et al. (2003) were able to infer shock velocities over much of the periphery, ranging from 430 to 960 km s^{-1} , consistent with X-ray inferences (Rakowski et al. 2003).

To model DEM L71, we used parameters deduced from *Chandra* observations (Rakowski et al. 2003), averaged over the entire blast wave since different subregions were fairly similar. We find a predicted 70/24 ratio in the absence of sputtering ($\tau = 0$) of about 2.3 (including only grains larger than $0.001 \mu\text{m}$ in radius), compared to the observed 5.1. Using an effective age of $1/3$ the Sedov age gave a value of 5.1. Table 3 also gives the total dust mass we derive, and the total IR luminosity produced by the model.

For 0548–70.4, both the east and west limbs and some bright knots of interior emission are visible at $24 \mu\text{m}$, but only the north half of the east limb is clearly detected at $70 \mu\text{m}$.

Only fluxes from this region were measured; the results are summarized in Table 1. Using a 1-D model for Coulomb heating of electrons by protons, we calculate a mean electron temperature in the shock region of $T_e \sim 0.66$ keV. A model using the postshock density of 0.72 cm^{-3} obtained by Hendrick et al. (2003) for the whole limb (including sputtering) gives too high a $70/24 \text{ } \mu\text{m}$ ratio. That ratio is very sensitive to density; we found that increasing n_p by a factor < 2.5 adequately reproduced the observed ratio. That fitted density appears in Table 2 and the corresponding results are in Table 3. Gas mass was derived from the X-ray emission measure of the east limb (Hendrick et al. 2003), scaled to the region shown in Figure 1, and using electron density in Table 2.

3.2. 0509–67.5 and 0519–69.0

Our other two objects are much smaller; X-ray data suggest young ages (Warren & Hughes 2004). Detections of light echoes (Rest et al. 2005) indicate an age of about 400 yr for 0509–67.5 and about 600 yr for 0519–69.0, with $\sim 30\%$ errors. Much higher shock velocities inferred by Ghavamian et al. (2006, in preparation) mean that plasma heating should be much more effective. Higher dust temperatures, hence lower $70/24 \text{ } \mu\text{m}$ ratios, should result. In fact, we did not detect either remnant at $70 \text{ } \mu\text{m}$, with upper limits on the ratio considerably lower than the other two detections (Table 1).

In the case of 0509-67.5, optical-UV observations fix only T_p , so we regarded the density n_p as a free parameter, fixing τ at $n_p t/3$ and finding T_e assuming no collisionless heating. Our $70 \text{ } \mu\text{m}$ upper limit gives a lower limit on n_p , shown in Table 2, as well as an upper limit on the total dust mass (Table 3).

The analysis of 0519-69.0 was identical to that done for 0509-67.5. However, for 0519-69.0 we divided the remnant up into two regions: the three bright knots (which we added together and considered one region, accounting for 20% of the total flux) and the rest of the blast wave. Optical spectroscopy (Ghavamian et al. 2006) allowed determination of parameters separately for the knots and the remainder. Again regarding n_p , T_e and τ as free parameters, we place lower limits on the post-shock densities and T_e , and upper limits on the amount of dust mass, including sputtering. For both remnants, density limits assume the effective sputtering age; if there is no sputtering at all, we obtain firm lower limits on density lower by less than a factor of 2.

4. Results and Conclusions

The IR emission in the Balmer-dominated SNRs in the LMC is spatially coincident with the blast wave. It is produced within the shocked ISM by the swept-up LMC dust heated in collisions with thermal electrons and protons. We find no evidence for infrared emission associated with either shocked or unshocked ejecta of these thermonuclear SNRs. While detailed modeling of small grains is required to make a quantitative statement, apparently little or no dust forms in such explosions, and any line emission produced by ejecta is below our detection limit. This is consistent with observations of Type Ia SNe where dust formation has never been observed. It is also consistent with the absence in meteorites of presolar grains formed in Type Ia explosions (Clayton & Nittler 2004).

The measured 70/24 μm MIPS ratios in DEM L71 and 0548-70.4, and the absence of detectable emission in the IRAC bands in all 4 SNRs, can be accounted for with dust models which include destruction of small grains. Without dust destruction, numerous small grains present in the LMC ISM (e.g., Weingartner & Draine 2001) would produce too much emission at short wavelengths when transiently heated to high temperatures by energetic particles. Destruction of small grains is required to reproduce the observed 70/24 μm MIPS ratios in DEM L71 and 0548-70.4: 90% of the mass in grains smaller than 0.03–0.04 μm is destroyed in our models. Even with this destruction, we infer pre-sputtering dust/gas mass far smaller than the 0.25% in the Weingartner & Draine model.

The two young remnants, 0509–67.5 and 0519–69.0, have been detected only at 24 μm , but our rather stringent upper limits at 70 μm suggest the presence of much hotter dust than in the older SNRs DEM L71 and 0548-70.4. Such hot dust is produced in our plane shock models only if the postshock electron densities exceed 1.6 cm^{-3} and 3.4–7.7 cm^{-3} in 0509–67.5 and 0519–69.0, respectively (Table 2). 0509–67.5 is asymmetric, and the quoted lower density limit needs to be reduced if an average postshock electron density representative of the whole SNR is of interest. We measure a flux ratio of 5 between the bright and faint hemispheres, depending primarily on the gas density ratio between the hemispheres, and on the ratio of swept-up ISM masses. For equal swept-up masses, our models reproduce the observed ratio for a density contrast of 3 or less; the actual density contrast is lower because more mass has been swept up in the brighter hemisphere. The nearly circular shape of 0509–67.5 also favors a low density contrast. The densities derived here are several times higher than an upper limit to the postshock density of 0.2 cm^{-3} obtained by Warren & Hughes (2004) who used hydrodynamical models of Dwarkadas & Chevalier (1998) to interpret *Chandra* X-ray observations of this SNR. The origin of this discrepancy is currently unknown. Possible causes include: (1) neglect of extreme temperature grain fluctuations in our dust models for 0509–67.5, (2) modification of the blast wave by cosmic rays as suggested for the Tycho SNR

by Warren et al. (2005), (3) contribution of line emission in the 24 μm MIPS band.

The measured 24 and 70 μm IR fluxes, in combination with estimates of the swept-up gas from X-ray observations, imply a dust/gas ratio a factor of several lower than typically assumed for the LMC. In order to resolve this discrepancy, one needs much higher dust destruction rates and/or a much lower dust/gas ratio in the pre-shock gas. Most determinations of dust mass come from higher-density regions, but Type Ia SNRs are generally located in the diffuse ISM, where densities are low. Both the dust content and the grain size distribution might be different in the diffuse ISM. In the Milky Way, the dust content is lower in the more diffuse ISM (e.g., Savage & Sembach 1996), most likely due to dust destruction by sputtering in fast SNR shocks (more prevalent at low ISM densities) and by grain-grain collisions in slower radiative shocks. Grain-grain collisions are the more likely destruction mechanism for large grains (Jones et al. 1994; Borkowski & Dwek 1995), so such grains might be less common in the diffuse ISM. Smaller grains are more efficiently destroyed by sputtering in SNRs, so dust destruction will be more efficient for a steeper preshock grain size distribution (more weighted toward small grains). This in combination with the lower than average preshock dust content mostly likely accounts for the observed deficit of dust in the Balmer-dominated SNRs in the LMC. Apparently dust in the ambient medium near these SNRs has been already affected (and partially destroyed) by shock waves prior to its present encounter with fast SNR blast waves. Spectroscopic follow-up is required in order to confirm preliminary conclusions presented in this work and learn more about dust and its destruction in the diffuse ISM of the LMC.

We thank Joseph Weingartner and Karl Gordon for discussions about dust in the LMC. This work was supported by NASA through Spitzer Guest Observer grant RSA 1265236, and by *Chandra* Archival Research grant SAO AR5-6007X. PFW acknowledges NSF grant AST-0307613.

REFERENCES

- Arendt, R. G. 1989, ApJS, 70, 181
- Bianchi, S., & Ferrara, A. 2005, MNRAS, 358, 379
- Borkowski, K. J., & Dwek, E. 1995, ApJ, 454, 254
- Borkowski, K. J., Harrington, J. P., Blair, W. P., & Bregman, J. D. 1994, ApJ, 435, 722
- Borkowski, K.J., Lyerly, W.J., & Reynolds, S.P. 2001, ApJ, 548, 820

- Clayton, D.D., & Nittler, L.R. 2004, ARAA, 42, 39
- Draine, B. T. 2003, ARAA, 41, 241
- Draine, B. T., & Lee, H. M. 1984, ApJ, 285, 89
- Dwarkadas, V. V., & Chevalier, R. A. 1998, ApJ, 497, 807
- Dwek, E. 1987, ApJ, 322, 812
- Dwek, E., & Arendt, R. G. 1992, ARAA, 30, 11
- Dwek, E., Foster, S. M., & Vancura O. 1996, ApJ, 457, 244
- Dwek, E., & Smith, R. K. 1996, ApJ, 459, 686
- Ghavamian, P., Raymond, J.C., Smith, R.C., & Hartigan, P. 2001, ApJ, 547, 995
- Ghavamian, P., Rakowski, C.E., Hughes, J.P., & Williams, T.B. 2003, ApJ, 590, 833
- Guhathakurta, P., & Draine, B. T. 1989, ApJ, 345, 230
- Hendrick, S.P., Borkowski, K.J., & Reynolds, S.P. 2003, ApJ, 593, 370
- Jones, A. P. 2004, in *Astrophysics of Dust*, Eds. A.N.Witt, C.C.Clayton and B.T.Draine (ASP Conf. Ser. 309), 347
- Jones, A. P., Tielens, A. G. G. M., Hollenbach, D. J., & McKee, C. F. 1994, ApJ, 433, 797
- Jurac, S., Johnson, R. E., & Donn, B. 1998, ApJ, 503, 247
- de Kool, M., Li, H., & McCray, R. 1998, ApJ, 503, 857
- Rakowski, C.E., Ghavamian, P., & Hughes, J.P. 2003, ApJ, 590, 846
- Rest, A., et al. 2005, Nature, 438, 1132
- Saken, J. M., Shull, J. M., & Fesen, R. A. 1992, ApJS, 81, 715
- Savage, B. D., & Sembach, K. R. 1996, ARA&A, 34, 279
- Smith, R.C., Kirshner, R.P., Blair, W.P., & Winkler, P.F. 1991, ApJ, 375, 652
- Tuohy, I. R., Dopita, M. A., Mathewson, D. S., Long, K.S., & Helfand, D. J. 1982, ApJ, 261, 473
- Warren, J. S., et al. 2005, ApJ, 634, 376

Warren, J. S. & Hughes, J. P. 2004, ApJ, 608, 261

Weingartner, J.C., & Draine, B.T. 2001, ApJ, 548, 296

This preprint was prepared with the AAS L^AT_EX macros v5.2.

Table 1. Measured Fluxes and Upper Limits^a

Object	8.0 μm	24 μm	70 μm
DEM L71	< 1.06	88.2 \pm 8.8	455 \pm 94
0548-70.4	< 3.82	2.63 \pm 0.30	19.9 \pm 4.7
0509-67.5	< 0.2	16.7 \pm 1.7	< 32.7
0519-69.0	< 0.9	92.0 \pm 9.2	< 121

^aAll fluxes (not color-corrected) in mJy. Limits are 3σ .

Table 2. Model Input Parameters

Object	T_e (keV)	T_p (keV)	n_p	n_e	Age (yrs.)	$\tau(10^{10} \text{ cm}^{-3} \text{ s})$	Ref.
DEM L71	0.65	1.1	2.3	2.7	4400	11	1, 2
0548-70.4	0.65	1.5	1.7	2.0	7100	12	3, 4
0509-67.5	1.9	89	> 1.4	> 1.6	400	0.59	4, 5
0519-69.0 ^a	2.1	36	> 2.8	> 3.4	600	1.8	4, 5
0519-69.0 ^b	1.0	4.2	> 6.4	> 7.7	600	4.0	4, 5

^aFainter portions of remnant

^bThree bright knots

Note. — Densities are post-shock. References: (1) Rakowski et al 2003; (2) Ghavamian et al 2003; (3) Hendrick et al 2003; (4) Ghavamian et al 2006, in preparation; (5) Rest et al. 2005

Table 3. Model Results

Object	70/24 (0)	70/24 sput.	70/24 obs.	$T(\text{dust})(\text{K})$	Dust Mass	% destr.	dust/gas	L_{36}
DEM L71	2.3	5.1	5.1	55–65	0.034	35	4.2×10^{-4}	12
0548-70.4	2.7	7.6	7.6	53–62	0.0018	40	7.5×10^{-4}	2.1
0509-67.5	< 2.0	< 2.0	< 2.0	66–70	$< 1.1 \times 10^{-3}$	> 18
0519-69.0 ^a	< 1.3	< 1.3	< 1.3	72–77	$< 2.7 \times 10^{-3}$	> 34
0519-69.0 ^b	< 1.3	< 1.3	< 1.3	73–86	$< 6.4 \times 10^{-4}$	> 38

^aFainter portions of remnant

^bThree bright knots

Note. — Column 2: model prediction without sputtering; column 3, including sputtering with $\tau = n_p t / 3$; column 4, observations; column 5, for 0.02–0.1 μm grains; column 6, mass of dust currently observed (after sputtering), in M_\odot ; column 7, percentage of original dust destroyed; column 8, ratio of swept-up dust to gas masses; column 9, $L_{36} \equiv L_{IR} / 10^{36} \text{ erg s}^{-1}$.

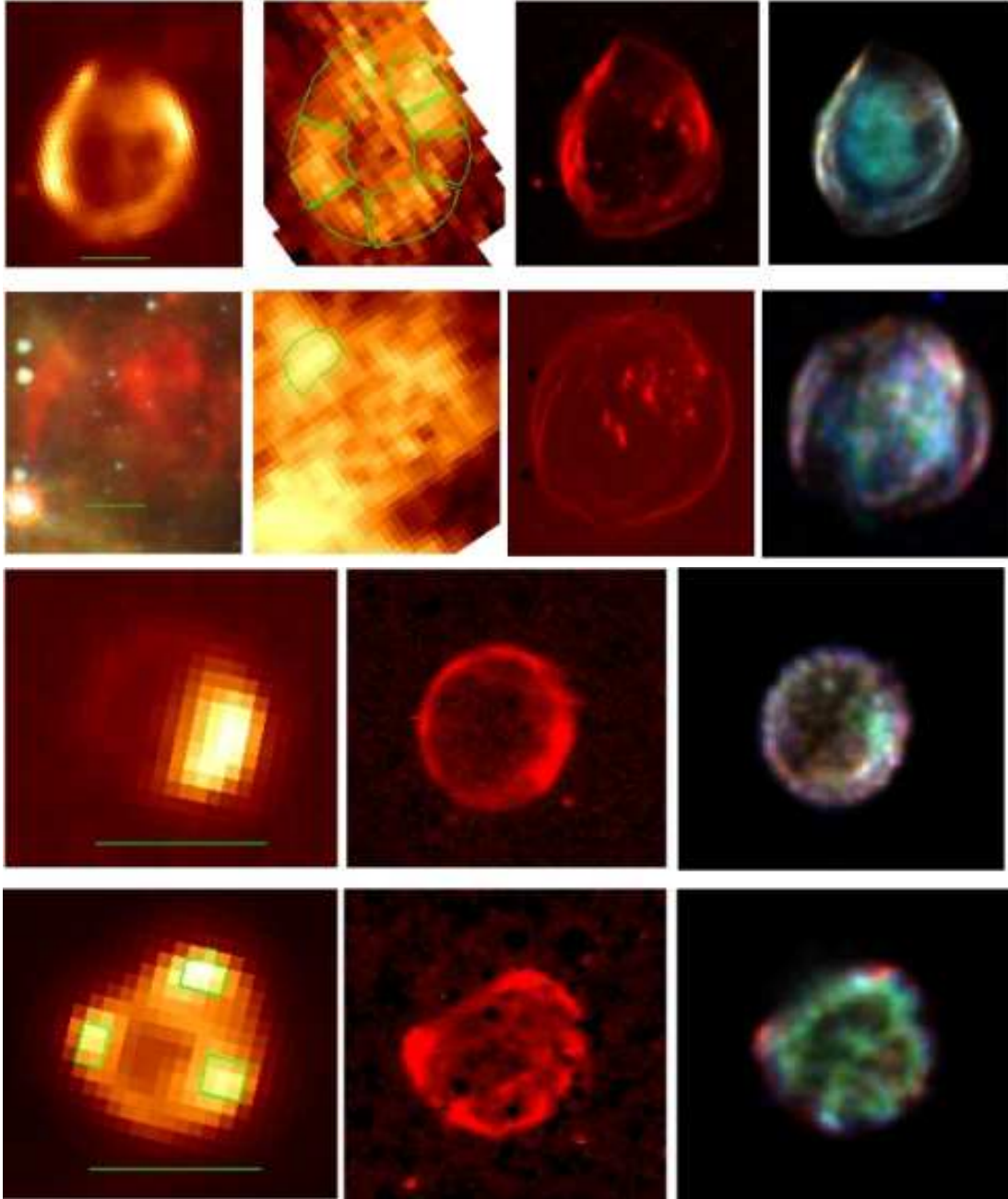


Fig. 1.— Top row: DEM L71 at 24 and 70 μm , $\text{H}\alpha$, and X-ray (red, 0.3 – 0.7 keV; green, 0.7 – 1.0 keV; blue, 1.0 – 3.5 keV; smoothed with 1 pixel Gaussian). Second row: 0548–70.4 with red, 24 μm ; green, IRAC 8.0 μm ; blue μm , IRAC 5.8 μm ; 70 μm ; $\text{H}\alpha$, and X-ray image as for DEM L71, smoothed with a 2 pixel Gaussian. Third row: 0509–67.5 at 24 μ , $\text{H}\alpha$, and X-ray: red, 0.3 – 0.7 keV; green, 0.7 – 1.1 keV and blue, 1.1 – 7.0 keV, Fourth row: 0519–69.0, as in third row. Half-arcmin scales are shown for each SNR.